



# A finite element study on residual stress stability and fatigue damage in high-frequency mechanical impact (HFMI)-treated welded joint



Eeva Mikkola <sup>\*</sup>, Heikki Remes, Gary Marquis

Aalto University, Department of Mechanical Engineering, P.O. Box 14300, FI-00076 Aalto, Finland

## ARTICLE INFO

### Article history:

Received 7 April 2016

Received in revised form 12 September 2016

Accepted 15 September 2016

Available online 16 September 2016

### Keywords:

High-frequency mechanical impact (HFMI)

Welded joints

Residual stresses

Variable amplitude loading

## ABSTRACT

Fatigue improvement from high-frequency mechanical impact (HFMI) is considered to rely on compressive residual stresses, improved weld toe geometry and localized strain hardening at the weld toe. Of these, the existence of compressive residual stresses is generally assumed critical for the effectiveness of the method. In this study, the influence of stress ratio and peak loads on residual stress relaxation and fatigue damage in as-welded and HFMI-treated S700 transverse attachments was investigated. Elastic-plastic stress-strain response for as-welded and HFMI-treated conditions was simulated considering the effects of initial residual stress distribution, local geometry and local material properties. Relative fatigue damage was estimated using the Smith-Watson-Topper parameter. Full residual stress relaxation was observed for a stress ratio of 0.5 and a compressive overload of 0.6 times the nominal yield strength. The fatigue damage assessment showed benefit from HFMI with respect to the as-welded state for all simulated load conditions. The results are consistent with experimentally observed behaviour. The step-wise analysis indicated that the remaining benefit after residual stress relaxation was due to geometry improvement and strain hardening.

© 2016 Elsevier Ltd. All rights reserved.

## 1. Introduction

High-frequency mechanical impact (HFMI) has emerged as an effective and user-friendly method for improving the fatigue strength of welded steel structures. HFMI techniques use cylindrical indenters, which are accelerated against the component surface with high frequency of >90 Hz [1]. The resulting local plastic deformation induces compressive residual stresses, improves weld toe geometry and strain-hardens the surface region. As a result, the fatigue crack initiation life is increased for these joints. Recently, fatigue assessment guidelines [2] together with procedures and quality assurance guidelines [1] for HFMI-treated welded steel structures have been proposed. The fatigue assessment guidelines are mainly based on small scale specimens subjected to constant amplitude (CA) loading and a stress ratio  $R = 0.1$  [3,4] and the existing IIW recommendations for post-weld improvement of steel and aluminium structures [5].

The effectiveness of different peening methods, including HFMI, is generally assumed to depend on the existence of compressive residual stresses [5]. These beneficial residual stresses can relax due to peak stresses and high mean stresses [6,7]. Welded

structures in service frequently experience these types of loads. Previous studies [8–10] have confirmed that the benefit from HFMI decreases with increasing stress ratio. High peak stresses, as single incidents or as a part of service loading, have also been shown to reduce the benefit from peening [11,12]. According to McClung [13], compressive loads tend to relax compressive residual stresses in proportion to their magnitude. High tensile stresses may result in reversed yielding or change the self-equilibrated tensile stresses outside the compressive residual stress zone and force the compressive stresses to relax. Relaxation due to a single peak load is typically considered more effective than gradual cyclic relaxation [13]. Current International Institute of Welding (IIW) fatigue design recommendations on post-weld improvement take residual stress relaxation into account by limiting allowable nominal stresses in these structures [5]. However, previous work [14], where available experimental high stress ratio and variable amplitude (VA) loading data were analysed, has indicated that the proposed peak stress limit for HFMI-treated joints subjected to fully-reversed loading [2] is too conservative in the case of variable amplitude (VA) loading.

It is understood that high stress ratios and peak stresses can reduce the benefit from HFMI-treatment. However, under what exact conditions does residual stress relaxation occur, or what is the impact of geometry improvement and strain hardening on

<sup>\*</sup> Corresponding author.

E-mail address: [eeva.mikkola@vtt.fi](mailto:eeva.mikkola@vtt.fi) (E. Mikkola).

### Nomenclature

|               |  |                  |                               |
|---------------|--|------------------|-------------------------------|
| $b$           | fatigue strength exponent                              | $\varepsilon'_f$ | fatigue ductility coefficient |
| $c$           | fatigue ductility exponent                             | $\nu$            | Poisson's ratio               |
| $C, \gamma$   | characteristic coefficients for kinematic hardening    | $\sigma$         | stress                        |
| $E$           | elastic modulus  | $\sigma'_f$      | fatigue strength coefficient  |
| $f_y$         | nominal yield strength                                 |                  |                               |
| $k_y$         | initial yield stress in tension at zero plastic strain |                  |                               |
| $2N_f$        | number of reversals to failure                         |                  |                               |
| $P_{SWT}$     | Smith-Watson-Topper parameter                          |                  |                               |
| $Q, a$        | characteristic coefficients for isotropic hardening    |                  |                               |
| $r$           | weld toe radius  |                  |                               |
| $R$           | stress ratio ( $S_{min}/S_{max}$ )                     |                  |                               |
| $S$           | nominal stress   |                  |                               |
| $\alpha$      | thermal expansion coefficient                          |                  |                               |
| $\varepsilon$ | strain   |                  |                               |

### Subscripts and modifiers

|          |               |
|----------|---------------|
| $a$      | amplitude     |
| $max$    | maximum value |
| $mean$   | mean value    |
| $min$    | minimum value |
| $p$      | plastic       |
| $\Delta$ | range         |

fatigue improvement, is unclear. As residual stress relaxation depends on the relationship of the local stresses and the local yield strength [15], geometry improvement and the strain-hardened layer at the weld toe affect the relaxation behaviour [16]. In addition, because of the decrease in stress concentration at the weld toe, HFMI might improve the fatigue strength even in the absence of compressive residual stresses. Strain hardening may have a positive influence on fatigue performance, as HFMI has been shown to increase the high-cycle fatigue strength of steel [17]. As a result, local geometry and material properties in addition to initial residual stress field need to be taken into account when considering the effectiveness of HFMI-treatment in welded joints subjected to service loading.

Lihavainen and Marquis [18] proposed fatigue life calculation of HFMI-treated joints using local strain approach and linear elastic fracture mechanics (LEFM). Local strain approach was used to estimate fatigue crack initiation life and LEFM to estimate fatigue crack propagation life. In the local strain approach calculations, they accounted for compressive residual stresses and geometry improvement based on measured values. Base material behaviour was assumed. Leitner et al. [19] simulated both the welding and HFMI processes in S355 steel to obtain a full residual stress distribution in a butt joint. Local geometry was considered through a stress concentration factor. Stress and strain based approaches together with fracture mechanics were used to calculate the fatigue life under CA loading. Both studies focused on the development of calculation methods for HFMI-treated joints. Residual stress relaxation was not discussed. Tehrani Yekta et al. [20] used a strain-based fracture mechanics model to estimate the effects of variations in ultrasonic impact treatment (UIT) on fatigue improvement. Finite element analysis was used to evaluate the local stress concentration at the weld toe, whereas residual stresses and microhardness based local material behaviour were taken into account in a strain-based fracture mechanics step. They concluded that the effectiveness of HFMI was not particularly sensitive to different treatment parameters and that the residual stress level and local stress concentration were more critical with respect to fatigue than the local microhardness. Residual stress relaxation was not treated explicitly.

The aim of this study is to understand the influence of residual stress relaxation on fatigue damage in HFMI-treated welded joints. This is considered critical for the development of fatigue assessment guidelines for HFMI-treated joints. The study is a part of a larger research effort, where HFMI-treated and welded S700 steel longitudinal attachments were fatigue tested under VA loading [21] and where the influence of HFMI-treatment on cyclic properties of S700 steel was investigated by strain-controlled fatigue

testing of thin steel sheet specimens [17]. These studies provided experimental data on fatigue performance of HFMI-treated joints subjected to peak stresses, residual stress distributions and local weld toe geometry in as-welded (AW) and HFMI-treated conditions and the local material behaviour at an HFMI-treated weld toe. To investigate residual stress relaxation in HFMI-treated joints, local stress-strain response in AW and HFMI-treated S700 transverse non-load-carrying attachments was simulated. Initial residual stress state, weld toe geometry and local material properties were based on the experimental data discussed above [17,21]. Smith-Watson-Topper parameter was used to estimate the resulting relative fatigue damage at the weld toe.

## 2. Numerical analysis

Residual stress relaxation in as-welded and HFMI-treated S700 joints was simulated with finite element (FE) program Abaqus [22]. High-strength steel S700 was chosen, as it was used in previous experimental studies by the research group characterising the effects of HFMI-treatment [17,21]. In addition, the level of fatigue improvement in HFMI-treated joints has been shown to increase with increasing steel strength [4,23], which makes high-strength steels of interest. The applied residual stress distributions and local HFMI geometry were based on measurements from S700 longitudinal attachments [21], whereas the applied material properties were based on strain-controlled fatigue tests of thin steel sheet specimens in different material conditions [17]. The test specimens represented S700 base material, HFMI-treated S700 steel and coarse-grain HAZ in MAG-welded S700.

### 2.1. Simulated cases

A transverse non-load-carrying attachment subjected to axial loading was modelled using elastic-plastic finite elements. Axial loading was chosen, as it is a typical loading condition in bridge and ship superstructures. The effects of residual stresses, local geometry and material condition were separated by modelling the joint in four stages:

- (1) The AW condition assumed a tensile residual stress distribution and heat-affected zone (HAZ) material condition typical for an as-welded joint together with as-welded local weld toe geometry.
- (2) The RS (HFMI) condition, where RS signifies residual stresses, included the assumed compressive residual stress distribution due to HFMI but used the as-welded local weld toe geometry and HAZ material condition.

- (3) The RS + Geometry (HFMI) condition included the same residual stress distribution and material condition as in RS (HFMI) but assumed a typical local weld toe geometry following HFMI.
- (4) The full HFMI condition included the same conditions as RS + Geometry (HFMI) and additionally considered local material properties of the strain-hardened material.

The simulated conditions are summarized in Table 1.

The applied loading cases represent CA loading with different stress ratios and the effects of peak stresses during VA loading. The applied loading histories are summarized in Fig. 1 and Table 2. CA loading with stress ratios  $R = -1, 0$  and  $0.5$  was applied at two stress levels. The nominal stress ranges  $\Delta S$  were chosen based on available fatigue test data for transverse attachments [10]. The fatigue lives in [10] were in the region of  $4 \times 10^5$  cycles for  $\Delta S_2$  and  $2 \times 10^6$  cycles for  $\Delta S_1$  (see Table 2). 20 cycles were simulated in each case, as this resulted in approximately stable mean stress behaviour in all investigated cases. The applied peak load scenarios with constant  $R = -1$  are described in Fig. 1 and Table 2. First, both location and type of peak load were varied. Then, the effect of peak stress magnitude on residual stress relaxation was studied. The applied maximum and minimum nominal peak stresses  $S_{\max}$  and  $S_{\min}$  represent different critical cases in relation to nominal yield strength  $f_y$ :

- $0.45f_y$  corresponds to the proposed maximum stress amplitude limit for  $R = -1$  [2].
- $0.6f_y$  is close to peak stresses applied during VA loading in previous experimental work by Yildirim and Marquis [21].
- $0.8f_y$  corresponds to the existing maximum stress limit for hammer and needle peened joints [5].

For S700,  $f_y$  is 700 MPa. The applied CA loading level of 300 MPa is close to typical equivalent stress range levels used in VA testing by Yildirim and Marquis [21]. 20 CA loading cycles were applied in each case.

## 2.2. Finite element model

### 2.2.1. Global and local geometry

The modelled global geometry shown in Fig. 2(a) represents a non-load-carrying joint with double-sided transverse attachments. As the analysis concentrates on weld toe behaviour, root side lack-of-penetration was not modelled. Weld toe radius  $r = 0.25$  mm was chosen to represent normal AW quality [24]. Yildirim and Marquis [21] measured HFMI-groove radii, width and depth after four different HFMI-treatments and analysed the data statistically. Average radius  $r$  of 3.3 mm, depth of 0.2 mm and width of 3.8 mm were used to describe the HFMI-groove. The groove dimensions are in the recommended range corresponding to an optimum HFMI-groove [1].

### 2.2.2. Boundary conditions and meshing

Due to symmetry, a quarter of the transverse attachment was modelled in 2D, see Fig. 2(a). The axial load was applied at the

main plate edge on the right and translations and rotations along the symmetry lines shown in Fig. 2(a) where restricted. The applied local meshing for AW and HFMI weld toe geometries is shown in Fig. 2(b) and (c), respectively. Linear plane strain elements were used to constrain transverse contraction at the weld toe. As there was no eccentricity, quadrilateral and triangle plane strain elements were used everywhere in the model. Finite strain theory was applied to allow large displacements and material non-linearity. The minimum element size was 0.025 mm in the AW toe region and 0.1 mm in the HFMI-groove region. Global element size was 1 mm.

### 2.2.3. Elastic-plastic material behaviour

Fig. 3 shows the assumed material property regions for the modelled AW and HFMI-treated conditions. Remes [25] has shown that weld metal properties have a relatively small effect on simulated stress-strain behaviour at weld toe in the case of overmatching welds. As the HAZ strength in MAG welded S700 has been observed slightly lower than the base material (BM) and weld metal strengths [26], BM properties were applied to the weld metal region. Coarse-grain HAZ was considered most critical with respect to fatigue. Based on hardness measurements by Bracke et al. [26], the thickness of the coarse-grain HAZ region was estimated to be approximately 1 mm. Other HAZ regions with higher fatigue resistance were not modelled. The simplification of the transition from HAZ to BM was based on the results by Remes [25,27]. Remes compared a detailed model with multiple HAZ regions to a simplified one similar to the one used here. The observed difference between the homogeneous and inhomogeneous models was small as for a notch, the energy strain times stress is close to constant, as Neuber has shown. The HFMI region thickness of 1 mm was based on experimental results by Mikkola et al. [17]. Hardness measurements [28,29] have shown that the gradient between the material property regions in the HFMI-groove region is relatively steep. Therefore, intermediate regions between the different material property regions were not included in the modelling.

Combined nonlinear isotropic-kinematic hardening [30] was used to describe the elastic-plastic material behaviour. Nonlinear kinematic hardening is described by characteristic coefficients  $C$  and  $\gamma$ , where  $C$  is the initial kinematic hardening modulus and  $\gamma$  describes the decrease in  $C$  with increasing plastic deformation. The kinematic part of the model can account for reversed yielding, ratcheting and mean stress relaxation. Isotropic hardening is determined with characteristic coefficients  $Q$  and  $a$ , where  $Q$  gives the maximum change in yield surface size due to cyclic hardening or softening and  $a$  determines the rate at which the yield surface size changes. Elastic response was determined by elastic modulus  $E$  and Poisson's ratio  $\nu$ . The full material description consisted of elastic response, yield condition, hardening rule and flow rule. See Lemaitre and Chaboche [30] for further information.

Mikkola et al. [17] used thin steel sheet specimens to determine the cyclic response of S700 base material, coarse-grain HAZ in MAG welded S700 and HFMI-treated S700. These material conditions correspond to the local BM, HAZ and HFMI material regions in Fig. 3. Measured cyclic stress-strain response at half-life for S700 BM, HAZ and HFMI conditions were fitted to the combined nonlinear isotropic-kinematic hardening model. Data from one specimen per material condition was used. HFMI-1 condition in Mikkola et al. [17] was chosen to represent the strain hardened HFMI condition at weld toe. As most of the cyclic softening took place before half-life, cyclic softening after half-life was not taken into account and  $Q$  and  $a$  were assumed zero. A comparison of experimentally observed and assumed softening behaviour for the simulated 20 cycles at 0.6% strain showed that the difference between the two was insignificant. Kinematic hardening parameters were determined from the experimentally estimated cyclic stress-strain

**Table 1**

Simulated joint conditions with properties at weld toe i.e. the assumed crack initiation location. RS is residual stress.

|                      | Residual stresses | Notch geometry | Material condition |
|----------------------|-------------------|----------------|--------------------|
| AW                   | Tensile           | AW             | HAZ                |
| RS (HFMI)            | Compressive       | AW             | HAZ                |
| RS + Geometry (HFMI) | Compressive       | HFMI-groove    | HAZ                |
| Full HFMI            | Compressive       | HFMI-groove    | HFMI               |

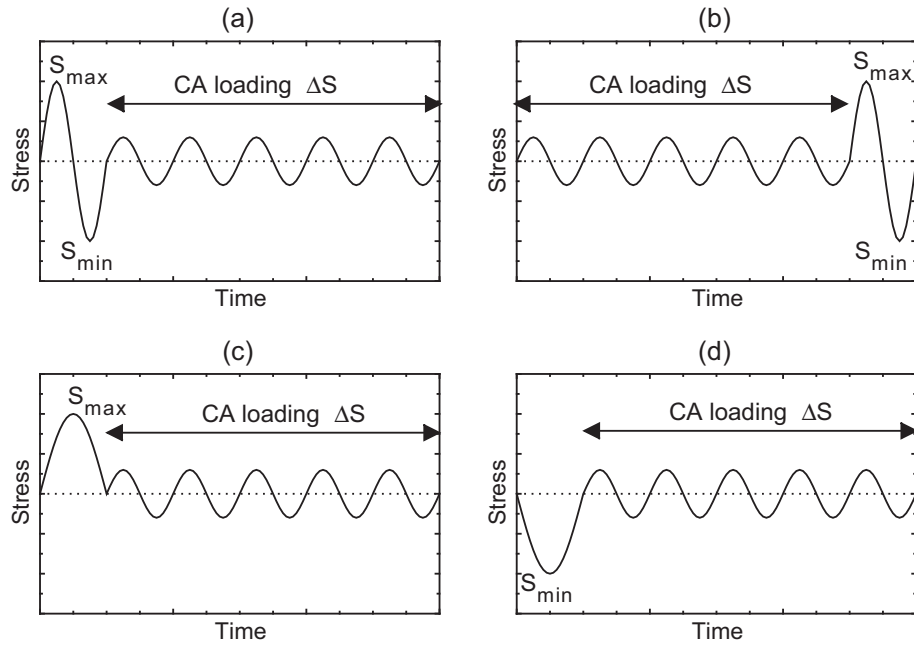


**Fig. 1.** A schematic representation of applied  $R = -1$  loading scenarios representing the effect of peak loads during VA loading. Totally 20 CA cycles are applied in each case.

**Table 2**  
Applied loading cases.

|                      | CA $R = -1$ or 0               | CA $R = 0.5$                   | Peak load cases ( $R = -1$ ) |                 |               |
|----------------------|--------------------------------|--------------------------------|------------------------------|-----------------|---------------|
|                      | $\Delta S_1, \Delta S_2$ (MPa) | $\Delta S_1, \Delta S_2$ (MPa) | $\Delta S$ (MPa)             | $S_{\max/\min}$ | Scenario      |
| AW                   | 300, 425                       | 250, 300                       | 300                          | $\pm 0.8f_y$    | Fig. 1(a)     |
| RS (HFMI)            | 300, 425                       | 250, 300                       | 300                          | $\pm 0.8f_y$    | Fig. 1(a)     |
| RS + Geometry (HFMI) | 300, 425                       | 250, 300                       | 300                          | $\pm 0.8f_y$    | Fig. 1(a)     |
| Full HFMI            | 300, 425                       | 250, 300                       | 300                          | $\pm 0.45f_y$   | Fig. 1(a)     |
|                      |                                |                                | 300                          | $\pm 0.6f_y$    | Fig. 1(a)     |
|                      |                                |                                | 300                          | $\pm 0.8f_y$    | Fig. 1(a)–(d) |

curves [22,30]. Stress  $\sigma$  as a function of plastic strain  $\varepsilon_p$  was calculated to determine  $k_y$ , which is the initial yield stress at zero plastic strain. The values for  $C$  and  $\gamma$  were then estimated from  $\sigma - k_y$  as a function plastic strain.  $C/\gamma$  corresponds to the maximum value of  $\sigma - k_y$  after which no further hardening occurs. The value for  $\gamma$  was estimated from

$$\sigma - k_y = \frac{C}{\gamma} [1 - \exp(-\gamma \varepsilon_p)]. \quad (1)$$

The fitted parameter values together with elastic modulus and Poisson's ratio values are provided in Table 3. A comparison of modelled and experimentally estimated half-life stress-strain curves and stress evolution is shown in Fig. 4. The experimental stress-strain curves represent average observed behaviour, whereas the modelled behaviour corresponds to single specimen behaviour. The differences between these two reflect therefore the observed variation in the test series. For strains above 1%, further hardening was limited as a conservative assumption due to lack of experimental data.

#### 2.2.4. Residual stresses

The applied longitudinal residual stress distributions were based on X-ray residual stress measurements. Yıldırım and Marquis [21] measured surface residual stresses in AW and HFMI-treated welded joints and Suominen et al. [31] measured residual stresses in HFMI-treated welded joints up to 2 mm depth using etching technique. All joints had S700 as base material. HFMI

residual stress distribution at 0–2 mm depth was estimated based on results by Suominen et al. [31]. The estimated minimum value was  $-319$  MPa at 0.5 mm depth. This is approximately 0.45% of the nominal yield strength of S700. At 2–10 mm depth, the values were chosen so that the distribution is self-equilibrated, as shown by the input distributions in Fig. 5. Based on surface measurements [31], it was estimated that the residual stress values are decreased to half at 3.5 mm distance. After that, the residual stresses quickly reduced to zero. The surface measurements showed that the absolute magnitude of surface residual stress in AW joints was similar to that found in HFMI-treated welded joints. This is to be expected since the magnitude of residual stresses is in relation to steel yield strength. As a result, a similar distribution with opposite magnitude residual stresses was used for the AW and HFMI conditions, as shown by the applied longitudinal residual stress distributions in Fig. 5. Transverse residual stresses following from Hooke's law were not calibrated to correspond to measured transverse stresses, as the longitudinal stresses in the direction of the applied axial load were considered critical with respect to fatigue.

The longitudinal residual stress distributions were introduced to FE program Abaqus as temperature fields [22]. The benefit of this approach is that it automatically resulted in equilibrium of stresses and strains, as the residual stress distributions were calculated in a thermal step before the cyclic load step. Normalized field distribution, field magnitude and thermal expansion coefficient were used to determine the temperature field. The residual stress distributions in Fig. 5 were normalized with respect to absolute



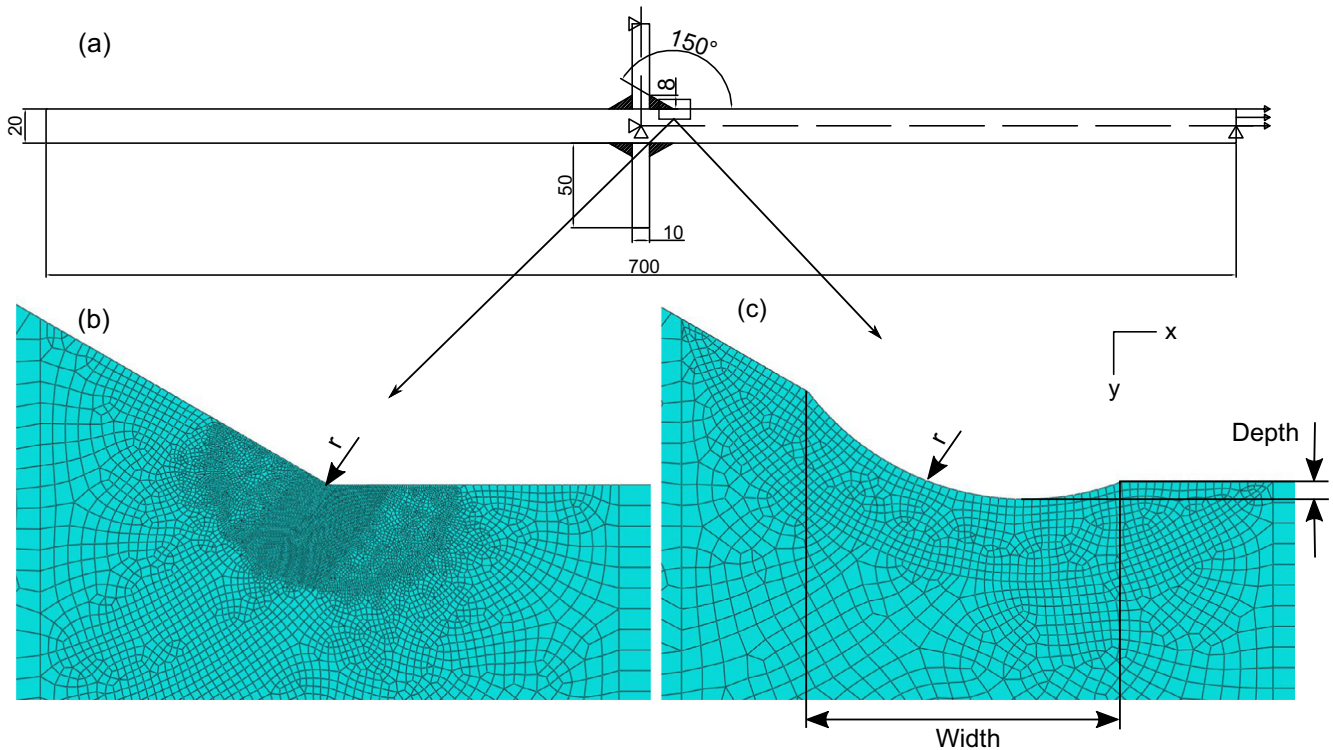


Fig. 2. (a) Analysed geometry with boundary conditions and applied axial loading. Local meshing for (b) AW condition and (c) HFMI-treated condition.

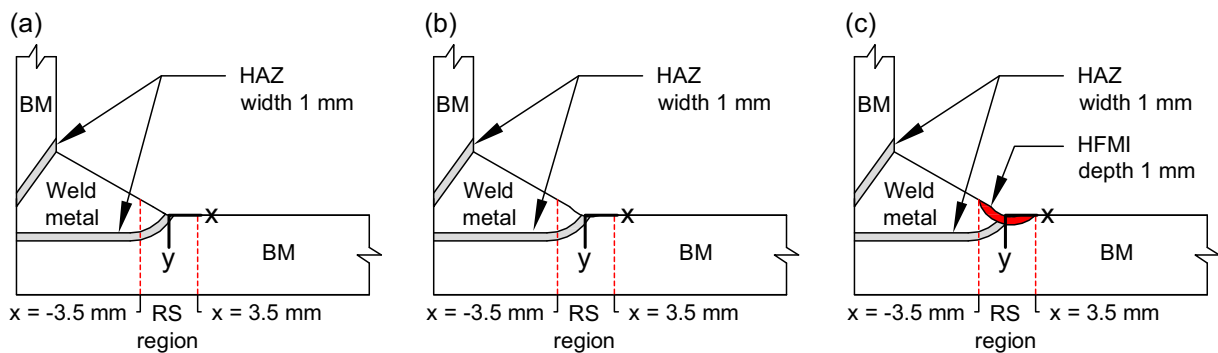


Fig. 3. Material property and residual stress (RS) regions for (a) AW and RS (HFMI), (b) RS + Geometry (HFMI) and (c) full HFMI joint conditions.

Table 3

Estimated material parameter values for the different material conditions representing half-life behaviour.

| Material condition | Elastic part |       | Nonlinear kinematic hardening |         |          | Isotropic hardening <sup>a</sup> |   |
|--------------------|--------------|-------|-------------------------------|---------|----------|----------------------------------|---|
|                    | E (GPa)      | $\nu$ | $k_y$ (MPa)                   | C (MPa) | $\gamma$ | Q (MPa)                          | a |
| BM                 | 210          | 0.3   | 550                           | 88,258  | 375      | 0                                | 0 |
| HAZ                | 210          | 0.3   | 431                           | 62,579  | 304      | 0                                | 0 |
| HFMI-1             | 210          | 0.3   | 606                           | 76,485  | 202      | 0                                | 0 |

<sup>a</sup> Stable half-life behaviour assumed in the analysis.

maximum stress values to obtain the required field distributions. A thermal expansion coefficient of  $\alpha = 1.2 \times 10^{-5}$ , which is typical for steel, was used for all material conditions. Based on the value of  $\alpha$ , a field magnitude of 130 was calibrated to yield maximum and minimum residual stress values corresponding to Fig. 5. Fig. 3 shows the coordinate system and lines according to which the residual distributions were applied. The temperature field was applied on an initial undeformed mesh. As the modelled transverse

attachment is symmetric, this did not result in any out-of-plane deformation in the thermal step.

The modelled residual stress distributions for the different joint conditions are shown in Fig. 5. In general, the modelled distributions followed the input distributions well. Close to  $y = 0$ , however, the distributions differed depending on local geometry and material condition. This was because of localized plasticity at the weld toe. The residual stresses for the AW condition and the HFMI con-

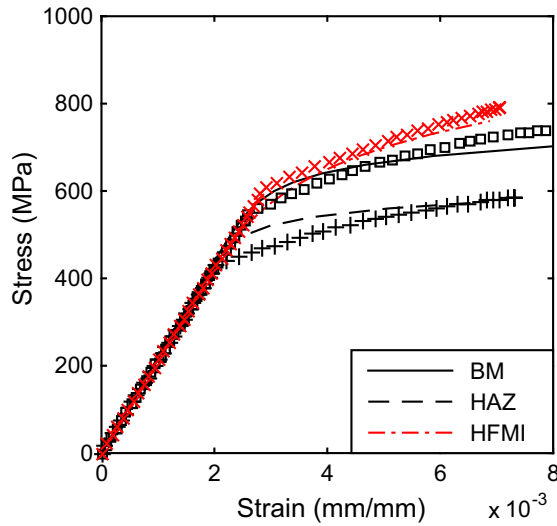


**Fig. 4.** Comparison of experimental and modelled half-life cyclic stress-strain curves representing local material conditions in an HFMI-treated welded joint. The lines signify behaviour estimated from experiments [17] and the symbols indicate model response with squares corresponding to BM, plus signs corresponding to HAZ and crosses corresponding to HFMI.

dition with compressive residual stresses [RS (HFMI)] were symmetrical. The HFMI model including residual stress and geometry effects [RS + Geometry (HFMI)] and the full HFMI condition had lower compressive residual stress values at  $y = 0$  than the HFMI condition with compressive residual stresses [RS (HFMI)]. This was due to a decrease in local stress concentration and an increase in local yield strength. As a result, the output residual stress distributions followed the input distributions more closely. With respect to the HFMI condition with compressive residual stresses [RS (HFMI)], the HFMI geometry effect simulated with RS + Geometry (HFMI) was slightly underestimated due to a decrease in compressive residual stress magnitude. The strain hardening effect simulated with full HFMI was not influenced by the residual stress distribution, as the difference in residual stress value between

the HFMI condition including residual stress and geometry effects [RS + Geometry (HFMI)] and full HFMI was relatively small. The differences in residual strains had little effect on the subsequent analysis, which considered only the resulting strain range.

### 2.3. Fatigue damage assessment

Smith-Watson-Topper parameter [32]

$$P_{SWT} = \sqrt{\varepsilon_a \sigma_{\max}}, \quad (2)$$

where  $\varepsilon_a$  is strain amplitude and  $\sigma_{\max}$  is maximum stress, was used to estimate relative fatigue damage. The parameter takes into account the effect of local mean stress and it has been successfully used to evaluate fatigue strength of welded joints, see e.g., Karakas [33] and Remes [25]. Strain and stress values at  $x = 0$  and  $y = 0.05$  mm (see Fig. 3) were used in the calculations based on previous work by Liinalampi et al. [34], who showed that an averaging depth of 0.05–0.1 mm was appropriate for fatigue assessment of welded thin plates with increased notch stresses. An example of a stress field in the analysis is shown in Fig. 6.  $x = 0$  gave values close to the absolute maximum value in all cases. Stress and strain values in the maximum principal stress direction were used. In the calculations, the first closed hysteresis loop was considered. For peak load cases starting with a peak cycle or reversal, the first closed hysteresis loop corresponded to the first CA cycle. For peak load cases ending with a peak cycle, only the local mean stress after the peak load cycle was considered, as there was no closed hysteresis loop after the peak load cycle.

$P_{SWT}$  is typically used as a means of correlating different mean stress conditions for a single material. Here the material condition was changing due to strain hardening. This made the comparison less straightforward. Eq. (3) gives the relationship of  $P_{SWT}$  and fatigue life

$$P_{SWT}^2 = \frac{\sigma_f^2}{E} (2N_f)^{2b} + \sigma_f' \varepsilon_f' (2N_f)^{b+c}, \quad (3)$$

where  $\sigma_f$  is the fatigue strength coefficient,  $b$  is fatigue strength exponent,  $\varepsilon_f'$  is fatigue ductility coefficient,  $c$  is fatigue ductility exponent and  $2N_f$  is reversals to failure [32]. Fig. 7 shows  $P_{SWT}$  as

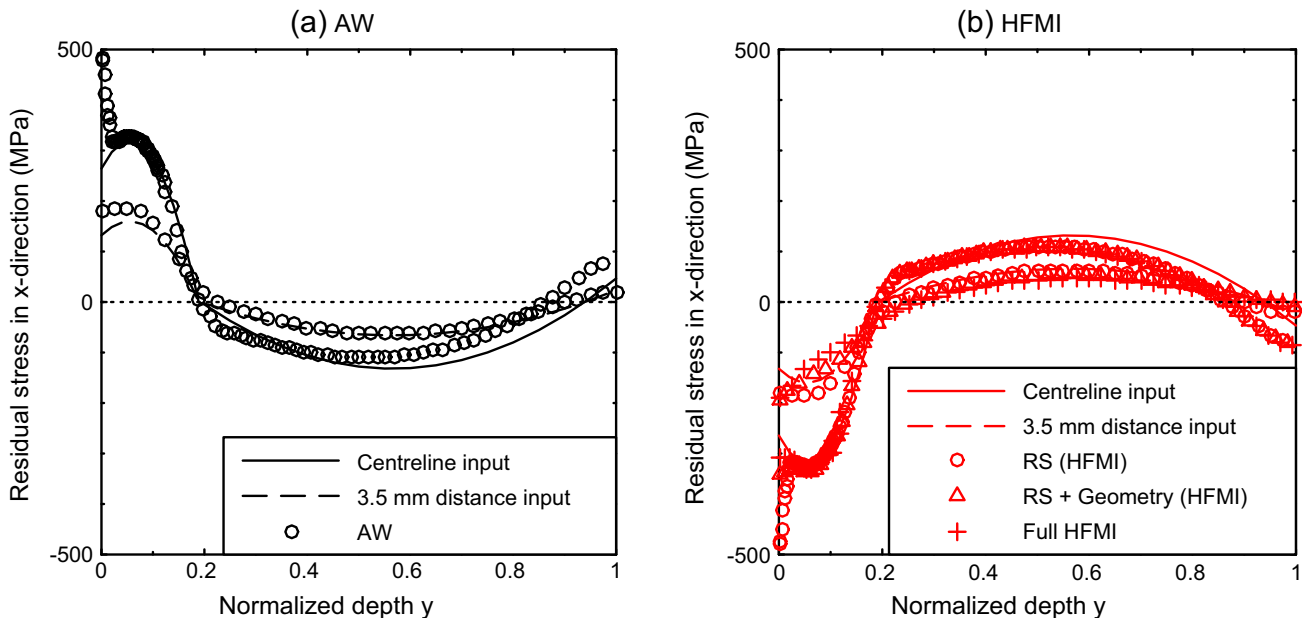


**Fig. 5.** Estimated and modelled residual stress distributions in the x-direction for (a) AW condition and (b) HFMI condition weld toe centreline and  $\pm 3.5$  mm distance from the centreline. Zero normalized depth equals weld toe surface. See Fig. 3 for x- and y-directions.

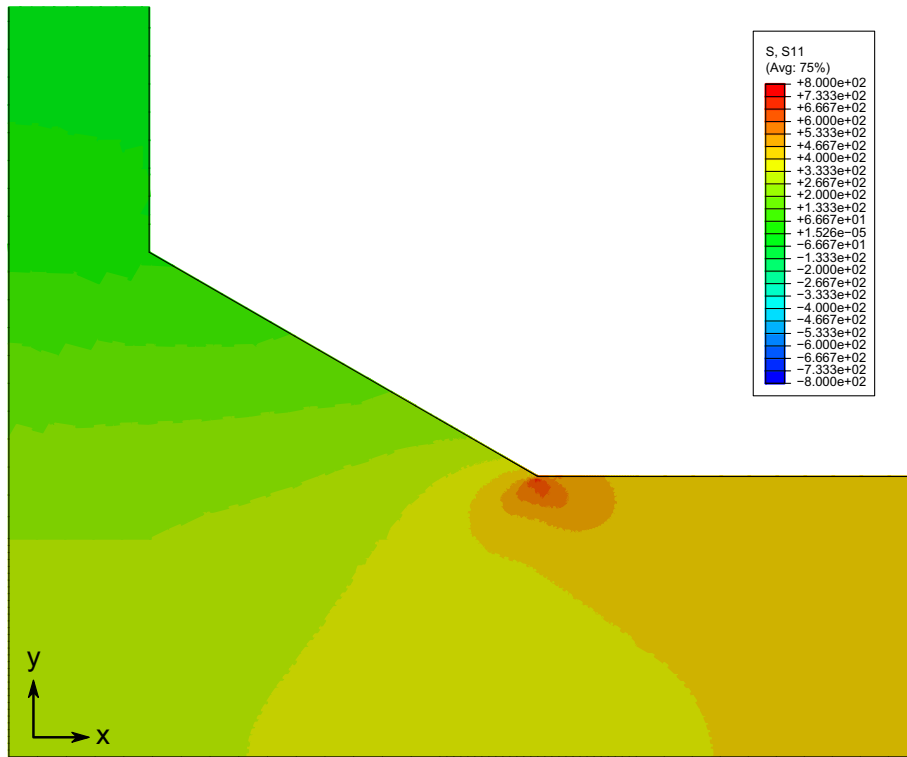


Fig. 6. An example of a stress field in the AW condition when  $S_{\max} = 212.5$  MPa.

a function of  $2N_f$  for BM, HAZ and HFMI material conditions. Material parameter values determined by Mikkola et al. [17] were used. Fig. 7 shows that the strain-hardened HFMI condition is expected to have higher fatigue resistance than the HAZ condition based on higher  $P_{SWT}$  value. This needs to be considered when comparing results for the geometry effect [RS + Geometry (HFMI)] and full HFMI models, as the weld toe material condition was changed from HAZ to HFMI in this step, see Table 1.

### 3. Results

#### 3.1. Local stress-strain response

The simulated stress-strain responses at the notch root for  $R = -1, 0$  and  $0.5$  CA loading with  $\Delta S_2$  is shown in Figs. 8–10.

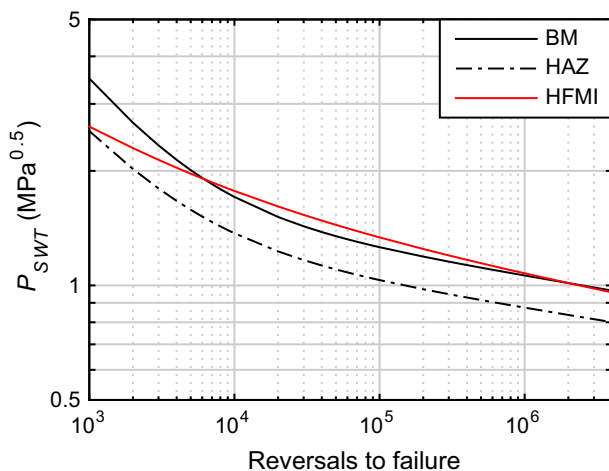
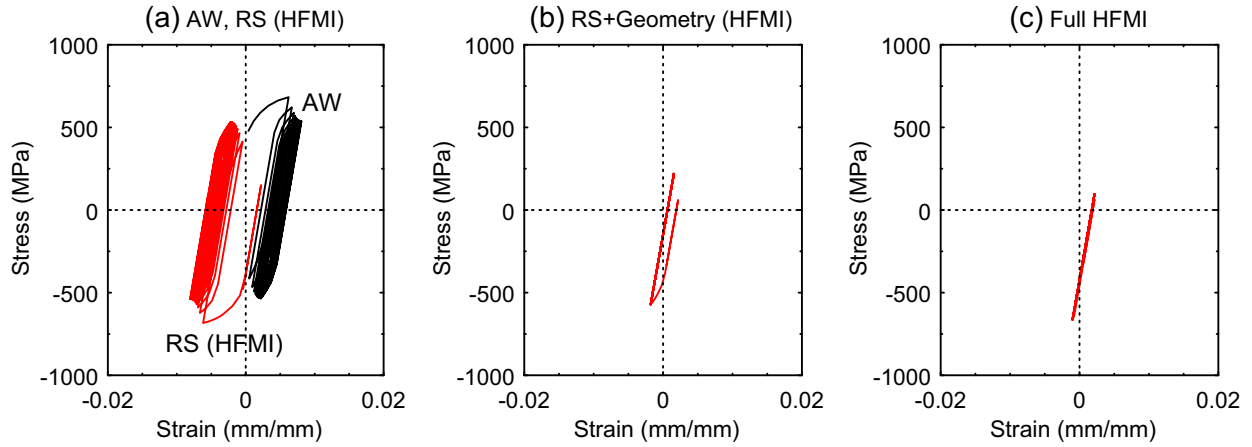


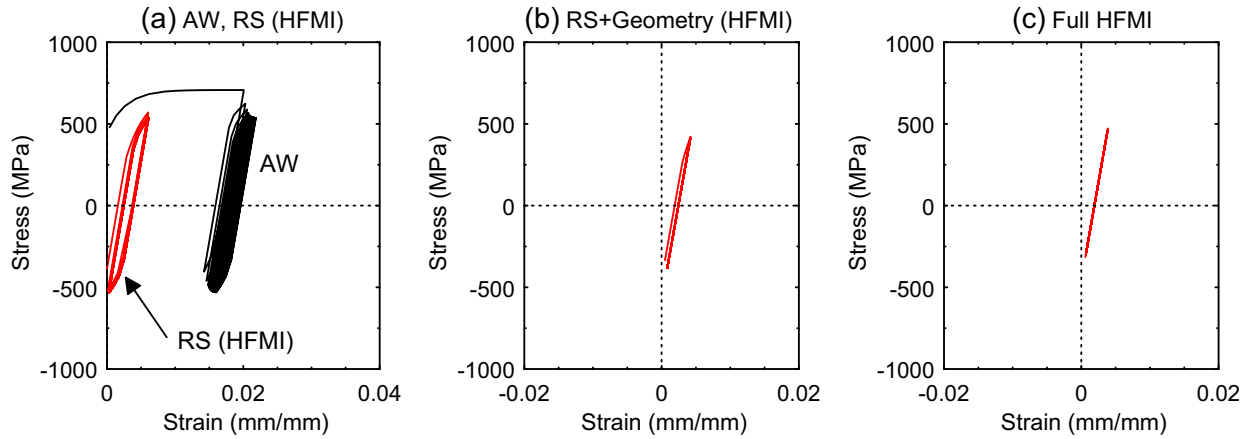
Fig. 7. Fatigue damage parameter as a function of reversals to failure for the different material conditions.

Table 4 summarizes these results by giving the strain range  $\Delta \epsilon$ , stress range  $\Delta \sigma$ , maximum stress  $\sigma_{\max}$  and mean stress  $\sigma_{\text{mean}}$  of the simulated stress-strain responses. Typically, the hysteresis loops were stable from the first cycle. Mean stress relaxation and ratcheting occurred in three cases - see Figs. 8(a) and 9(a). For these cases, Table 4 gives the change in maximum and mean stress from the first full hysteresis loop to the last full hysteresis loop. The stress and strain ranges remained approximately constant in all cases. The figures and table show that compressive residual stresses [RS (HFMI)] reduced the local mean and maximum stresses compared to AW condition, whereas geometry improvement [RS + Geometry (HFMI)] and strain hardening (full HFMI) reduced the level of yielding and the resulting stress and strain ranges. For  $R = 0$  and  $0.5$ , the strain hardening accounted for in the full HFMI condition tended to increase the local mean and maximum stresses because of higher local yield strength.

Fig. 8 shows that mean stress relaxation occurred in the AW and HFMI with compressive residual stress [RS (HFMI)] conditions when  $R = -1$ . As a result, the local mean stress after 20 cycles was close to zero for both joint conditions. When the geometry effect [RS + Geometry (HFMI)] and strain hardening effect (full HFMI) were taken into account, this was not observed, as both geometry improvement and strain hardening limited the level of yielding. In fact, the stress-strain response for the full HFMI with HFMI-induced strain hardening was approximately elastic. For  $R = 0$  shown in Fig. 9, the results were similar to those for  $R = -1$ . Residual stress relaxation occurred only in AW condition. In addition, the resulting mean and maximum stresses were higher for all joint conditions due to the increase of applied mean stress from  $R = -1$  to  $0$ . Fig. 10 and Table 4 show that compressive residual stresses provided little benefit for  $R = 0.5$ . Geometry improvement [RS + Geometry (HFMI)] and strain hardening (full HFMI) reduced, however, the local stress and strain ranges. For  $\Delta S_1$ , the decrease in nominal stress range reduced the local stress and strain range values resulting in stable hysteresis loop behaviour for all stress



**Fig. 8.** Simulated local stress-strain response for (a) AW and RS (HFMI), (b) RS + Geometry (HFMI) and (c) full HFMI under CA loading when  $R = -1$  and  $\Delta S_2 = 425$  MPa.



**Fig. 9.** Simulated local stress-strain response for (a) AW and RS (HFMI), (b) RS + Geometry (HFMI) and (c) full HFMI under CA loading when  $R = 0$  and  $\Delta S_2 = 425$  MPa.

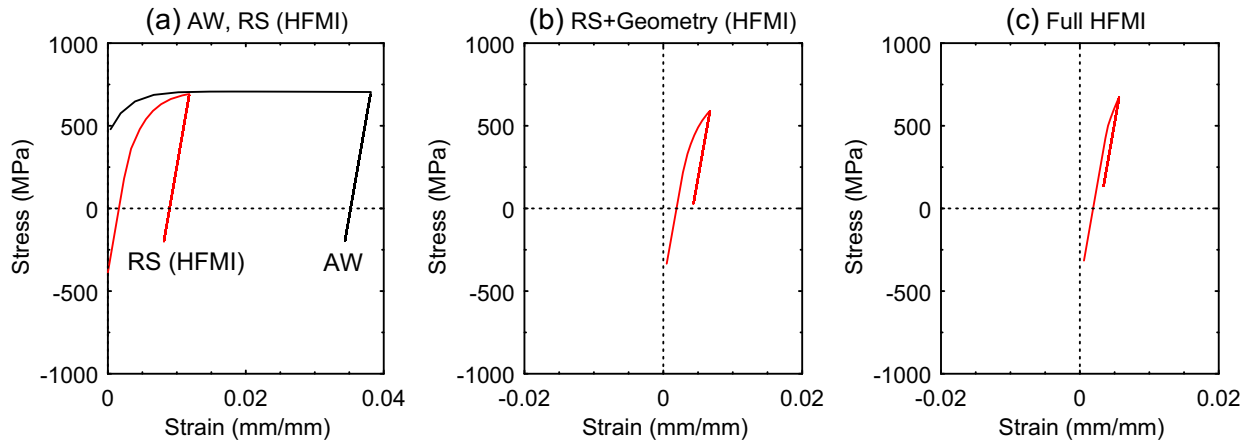


**Fig. 10.** Simulated local stress-strain response for (a) AW and RS (HFMI), (b) RS + Geometry (HFMI) and (c) full HFMI under CA loading when  $R = 0.5$  and  $\Delta S_2 = 300$  MPa.

ratios. The level of yielding was also reduced in all cases. For  $R = 0$  and  $\Delta S_1$ , the stress-strain response was approximately elastic for all HFMI joint conditions. The residual stresses did not relax significantly at low cyclic load levels because the local yield strength in HFMI-treated S700 steel was relatively high, as shown by Fig. 4. Ratcheting occurred only in conjunction with residual stress relaxation. Finally, since the maximum residual stress peak was located

at the weld toe, residual stress redistribution was only observed when relaxation at the weld toe region took place.

Fig. 11 compares full HFMI stress-strain response under different peak load sequences. The applied maximum and minimum stresses in each case were  $\pm 0.8f_y$  and the CA loading stress range was 300 MPa. Table 5 summarizes these results by giving the strain range  $\Delta \epsilon$ , stress range  $\Delta \sigma$ , maximum stress  $\sigma_{\max}$  and mean stress



**Table 4**

Summary of simulated stress-strain responses from Figs. 8–10 with CA loading. Arrows indicate change from first closed hysteresis loop to last closed hysteresis loop.

|  | $\Delta\epsilon$ (mm/mm) | $\Delta\sigma$ (MPa) | $\sigma_{\max}$ (MPa) | $\sigma_{\text{mean}}$ (MPa) |
|--|--------------------------|----------------------|-----------------------|------------------------------|
| CA loading with $R = -1$ and $\Delta S_2 = 425$ MPa  |                          |                      |                       |                              |
| AW   | 0.0062                   | 1098                 | 683 → 537             | 134 → 1                      |
| RS (HFMI)  | 0.0062                   | 1098                 | 414 → 532             | −135 → −3                    |
| RS + Geometry (HFMI)                                 | 0.0033                   | 791                  | 220                   | −176                         |
| Full HFMI  | 0.0032                   | 758                  | 96                    | −283                         |
| CA loading with $R = 0$ and $\Delta S_2 = 425$ MPa   |                          |                      |                       |                              |
| AW   | 0.0061                   | 1111                 | 707 → 537             | 151 → 3                      |
| RS (HFMI)  | 0.0059                   | 1085                 | 571 → 534             | 28 → −1                      |
| RS + Geometry (HFMI)                                 | 0.0034                   | 802                  | 421                   | 20                           |
| Full HFMI  | 0.0032                   | 769                  | 472                   | 88                           |
| CA loading with $R = 0.5$ and $\Delta S_2 = 300$ MPa |                          |                      |                       |                              |
| AW   | 0.0037                   | 898                  | 704                   | 255                          |
| RS (HFMI)  | 0.0037                   | 888                  | 692                   | 248                          |
| RS + Geometry (HFMI)                                 | 0.0024                   | 560                  | 590                   | 311                          |
| Full HFMI  | 0.0022                   | 536                  | 673                   | 405                          |

$\sigma_{\text{mean}}$  of the simulated stress-strain responses. For Fig. 11(b), where the simulation ended at a peak load cycle, only the end value corresponding to local mean stress is provided. In Fig. 11(a) and (b), the order of CA loading and the peak load cycle was changed. This had little effect on resulting local mean stress. Fig. 11(c) and (d) shows the difference between a compressive and a tensile overload. The compressive overload resulted in the same mean stress as the full peak load cycle in Fig. 11(a), as shown

by Table 5, whereas the tensile overload had little effect on the local mean stress. To see the effect of subsequent load cycles, a second peak load cycle was applied following the stress-strain response in Fig. 11(a). This increased the mean stress from 99 MPa to 182 MPa.

Fig. 12 and Table 6 give a comparison of different peak load magnitudes for full HFMI and AW conditions. All applied peak load magnitudes shifted the local mean stress. For  $S_{\max/\min} = \pm 0.45f_y$  in

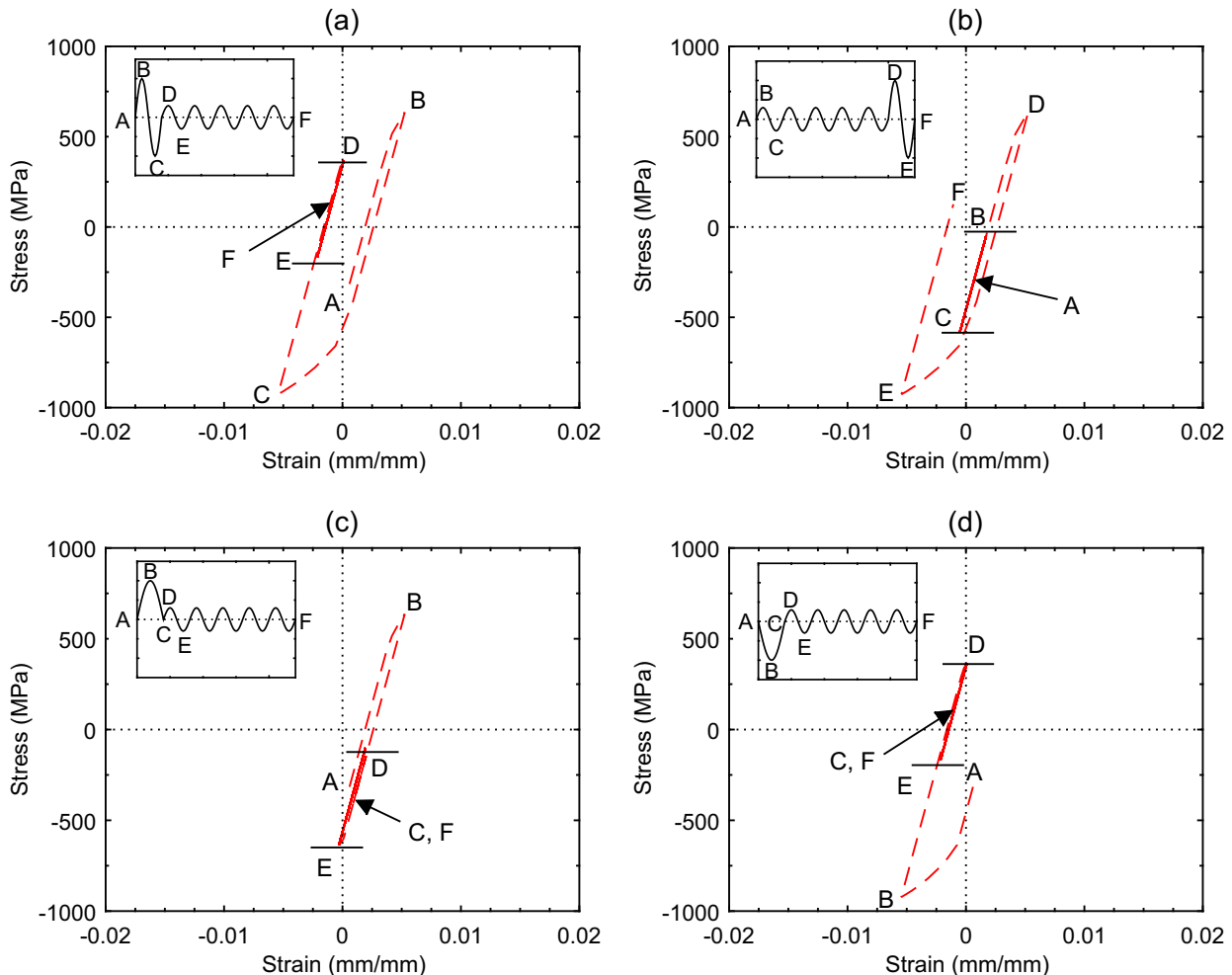


**Fig. 11.** Simulated local stress-strain response for full HFMI under different peak load sequences.  $R = -1$  and CA loading  $\Delta S = 300$  MPa. The absolute value of maximum stress is  $0.8f_y$  in each case.

**Table 5**

Summary of simulated stress-strain responses from Fig. 11 with different peak load scenarios. The provided values are for the CA loading cycles when available or at the end of the simulation.

|                              | $\Delta\epsilon$ (mm/mm) | $\Delta\sigma$ (MPa) | $\sigma_{\max}$ (MPa) | $\sigma_{\text{mean}}$ (MPa) |
|------------------------------|--------------------------|----------------------|-----------------------|------------------------------|
| OL cycle + CA                | 0.0022                   | 535                  | 366                   | 99                           |
| CA + OL cycle                | n/a                      | n/a                  | n/a                   | 126 <sup>a</sup>             |
| Tensile OL reversal + CA     | 0.0022                   | 535                  | −101                  | −368                         |
| Compressive OL reversal + CA | 0.0022                   | 535                  | 366                   | 99                           |

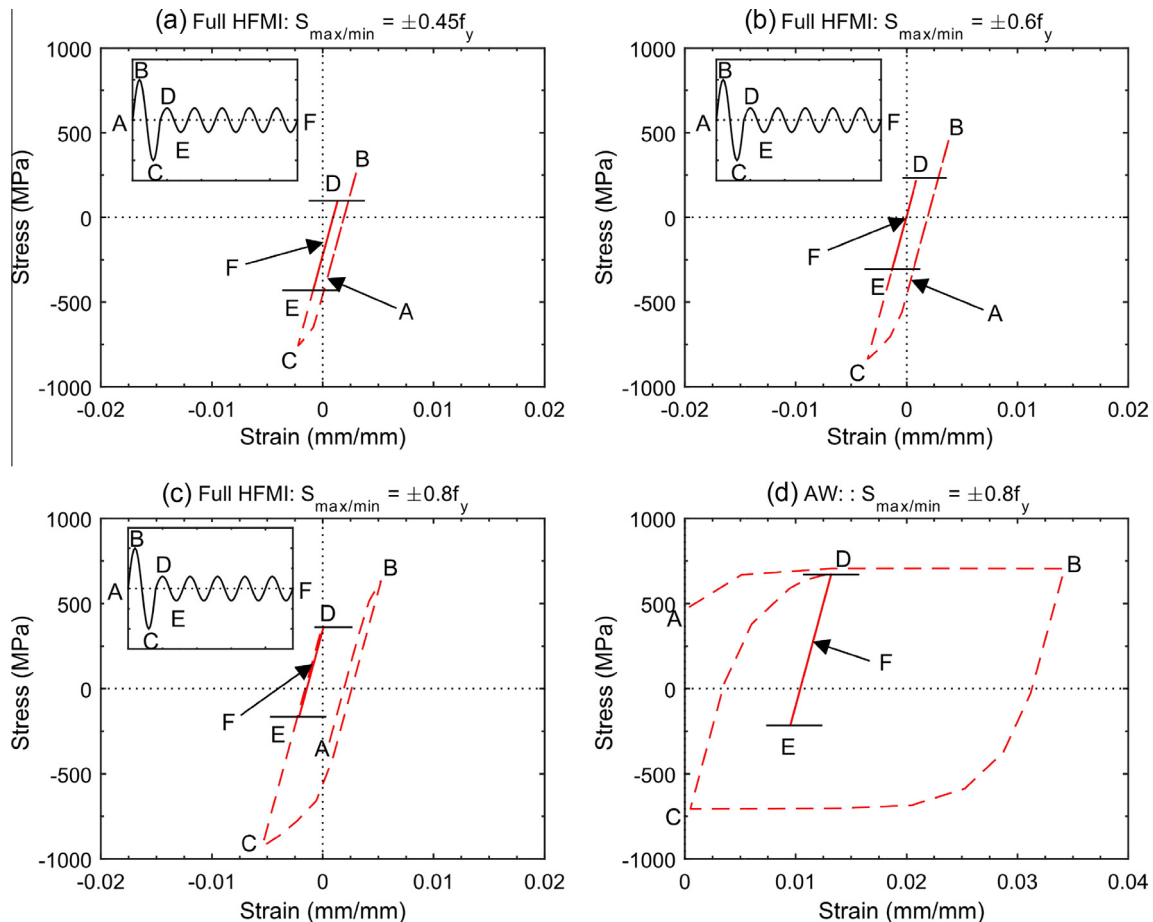
<sup>a</sup> Does not represent a closed hysteresis loop.

Fig. 12(a), residual stress relaxation was limited and local mean stress remained compressive. The second peak load magnitude of  $S_{\max/\min} = \pm 0.6f_y$  shown in Fig. 12(b) shifted the local mean stress close to zero indicating nearly full residual stress relaxation. For  $S_{\max/\min} = \pm 0.8f_y$  in Fig. 12(c), the local mean stress shifted to tension. At 0.1 mm depth, however, the local mean stress was zero also for this peak load magnitude. A peak load of  $S_{\max/\min} = \pm 0.8f_y$  was applied also for AW. Fig. 12(d) shows that in this case, the local mean stress shifted towards zero but remained tensile. As a result, the AW local mean stress was higher than the full HFMI local mean stress even after residual stress relaxation. In addition, the stress and strain ranges for the simulated AW case were higher than for the corresponding full HFMI case.

### 3.2. Fatigue damage

Fig. 13 shows the estimated fatigue damage parameter values for CA loading with stress ratios  $R = -1, 0$  and  $0.5$ . For full HFMI

under  $R = -1$  and  $\Delta S = 300$  MPa, the simulated maximum stress value was compressive, which corresponds to zero  $P_{SWT}$  value. As this is unrealistic, a modified approximate value was derived as  $P_{SWT}^* = P_{SWT} \times (300 \text{ MPa}/425 \text{ MPa})$  and used to correlate the results for the two nominal stress ranges. Fig. 13 shows that the benefit from HFMI decreased with increasing nominal stress range and increasing stress ratio. Geometry improvement decreased relative fatigue damage in all cases, whereas compressive residual stresses decreased the  $P_{SWT}$  values for  $R = -1$  and  $0$ . For  $R = 0.5$ , compressive residual stresses provided little benefit. In addition, it should be noted that the  $P_{SWT}$  analysis considered only the first closed hysteresis loop and therefore did not take into account mean stress relaxation. As a result, the residual stress effect between AW condition and HFMI condition with compressive residual stresses [RS (HFMI)] for  $\Delta S = 425$  MPa in Fig. 13(a) and (b) might be overestimated. The influence of strain hardening considered in the full HFMI condition was not as clear as the benefit from compressive residual stresses [RS (HFMI)] and geometry improvement [RS

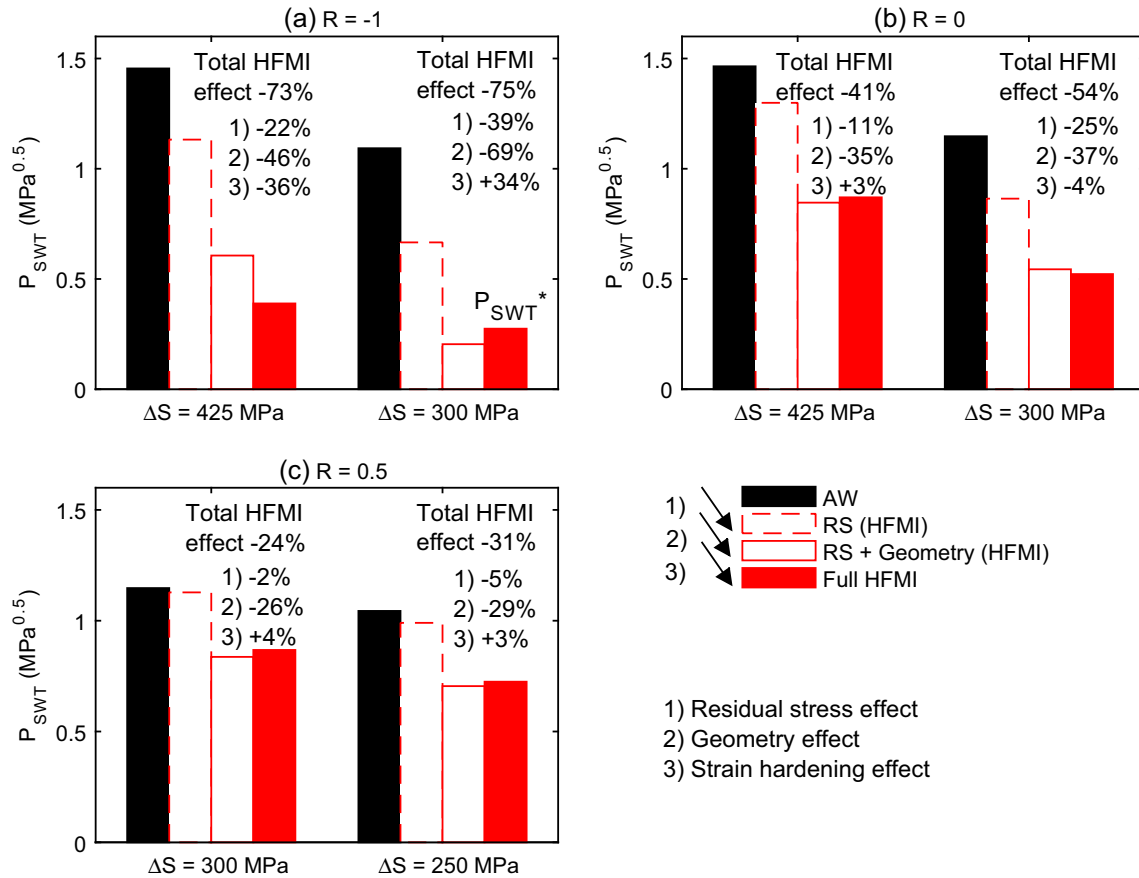


**Fig. 12.** Simulated local stress-strain response for (a)–(c) full HFMI and (d) AW conditions. The CA loading is with  $R = -1$  and  $\Delta S = 300$  MPa.

**Table 6**

Summary of simulated stress-strain responses from Fig. 12 with different magnitude peak loads. The provided values correspond to the CA loading cycles.

|                                     | $\Delta\epsilon$ (mm/mm) | $\Delta\sigma$ (MPa) | $\sigma_{\max}$ (MPa) | $\sigma_{\text{mean}}$ (MPa) |
|-------------------------------------|--------------------------|----------------------|-----------------------|------------------------------|
| Full HFMI $S_{\max/\min} = 0.45f_y$ | 0.0022                   | 535                  | 99                    | −168                         |
| Full HFMI $S_{\max/\min} = 0.6f_y$  | 0.0022                   | 535                  | 219                   | −49                          |
| Full HFMI $S_{\max/\min} = 0.8f_y$  | 0.0022                   | 535                  | 367                   | 100                          |
| AW $S_{\max/\min} = 0.8f_y$         | 0.0037                   | 892                  | 676                   | 231                          |

**Fig. 13.** Estimated fatigue damage parameter values for CA loading with (a)  $R = -1$ , (b)  $R = 0$  and (c)  $R = 0.5$ .  $P_{SWT}^* = P_{SWT} \times (300 \text{ MPa}/425 \text{ MPa})$  is a modified value based on the  $P_{SWT}$  value for  $\Delta S = 425 \text{ MPa}$ .

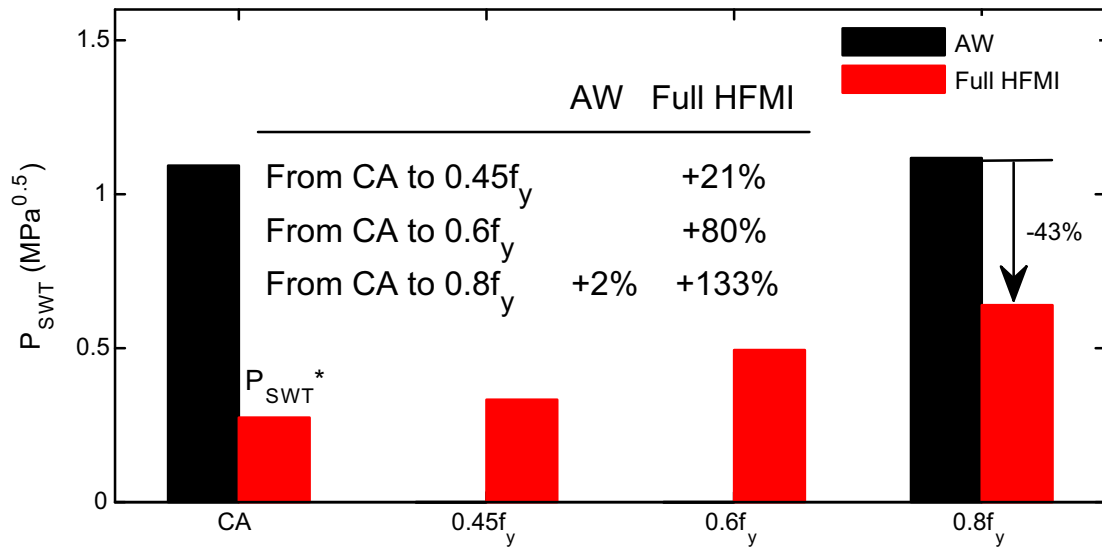
+ Geometry (HFMI)]. In four out of six cases, fatigue damage was increased from the HFMI condition including the residual stress and geometry effects [RS + Geometry (HFMI)] to the full HFMI condition. This was due to high maximum stress values resulting from high local yield strength. However, as discussed in Section 2.3, the strain-hardened HFMI condition included in the full HFMI condition is expected to have higher fatigue resistance than the HAZ condition assumed for AW and the other HFMI joint conditions. Fig. 7 shows that for  $P_{SWT} = 0.8 \text{ MPa}^{0.5}$ , for example, the fatigue life would be increased by a factor of 13 from HAZ to HFMI. Based on this, the same fatigue damage parameter value is expected to result in a longer fatigue crack initiation life for the full HFMI condition than the AW condition.

Fig. 14 compares the estimated  $P_{SWT}$  values for the peak load cases from Fig. 12. Fatigue damage was calculated from the CA loading cycles summarized in Table 6. As previously, a modified value  $P_{SWT}^*$  was used for full HFMI under  $R = -1$  and  $\Delta S = 300 \text{ MPa}$ . Fig. 14 shows that fatigue damage increased with increasing peak stress magnitude. Nevertheless, the estimated fatigue damage for full HFMI was still low relative to the fatigue damage for AW. Additional simulations with  $S_{\max/\min} = \pm 0.8f_y$  were run to separate the residual stress, geometry and strain hardening effects in the case

of an overload simulation. The results indicated little benefit from residual stresses and considerable benefit from geometry improvement, as in the case of  $R = 0.5$  CA loading. Unlike for  $R = 0.5$ , strain hardening provided benefit in the simulated overload case. This was due to increase in yield strength from the assumed HAZ condition to the assumed HFMI condition, which limited the yielding and thus the shift in local mean stress.

#### 4. Discussion

Residual stress relaxation in welded and HFMI-treated welded joints was simulated based on previous experimental work by Yıldırım and Marquis [21] and Mikkola et al. [17]. Yıldırım and Marquis [21] measured surface residual stresses before and after VA loading and observed full residual stress relaxation. The applied peak compressive stresses in these tests were approximately  $0.54f_y$  and  $0.7f_y$ . In the simulations, all peak loads resulted in residual stress relaxation for the full HFMI joint condition. For  $S_{\max/\min} = \pm 0.45f_y$ , residual stress relaxation was very limited. For  $S_{\max/\min} = \pm 0.6f_y$ , on the other hand, local mean stress was shifted close to zero indicating full residual stress relaxation. This is con-



**Fig. 14.** Estimated fatigue damage parameter values for full HFMI and AW with different peak load magnitudes.  $P_{SWT}^* = P_{SWT} \times (300 \text{ MPa}/425 \text{ MPa})$  is a modified value based on the  $P_{SWT}$  value for  $\Delta S = 425 \text{ MPa}$ .

trary to the suggestion by McClung [13] that residual stresses rarely relax to zero, but in line with experimental observations by Yıldırım and Marquis [21]. The simulations with different load scenarios showed that the beneficial compressive residual stresses relaxed due to the compressive part of the overload cycle, as expected [13], whereas the applied tensile overload had little effect on local mean stress. In addition, the influence of a second peak stress cycle was much smaller than that of the first peak stress cycle, as indicated by McClung [13]. The relative fatigue damage increased with increasing peak stress magnitude due to residual stress relaxation. However, benefit from HFMI-treatment remained even for  $S_{min} = -0.8f_y$  with respect to similarly loaded AW state. This is in agreement with experimentally observed benefit from HFMI-treatment under VA loading [14,21,35,36]. Similarly, both the fatigue damage analysis and experiments [8–10] have indicated benefit from HFMI under  $R = 0.5$  CA loading.

The computed  $P_{SWT}$  values shown in Fig. 13 indicated that the benefit observed for  $R = 0.5$  after residual stress relaxation was due to the geometry effect. Geometry improvement decreased relative fatigue damage in all cases by reducing local stress concentration at the weld toe. This decreased the local stresses and limited the level of residual stress relaxation. The fatigue damage analysis using  $P_{SWT}$  showed little benefit from strain hardening for CA loading. However, Fig. 7 indicated a significant increase in fatigue resistance from the assumed AW weld toe condition to the assumed strain-hardened weld toe condition. In addition, cold-working in general is known to increase the high-cycle fatigue strength of steels [37]. Therefore, strain hardening is expected to delay fatigue crack initiation in HFMI-treated weld joints. For the overload scenario, on the other hand, the relative fatigue damage analysis indicated benefit from strain hardening. This was because of high local yield strength that limited the level of residual stress relaxation. The observed benefit is in agreement with observations by Tehrani Yekta et al. [20], who analysed the effect of local hardness in the UIT-affected region using a strain-based fracture mechanics model. Their results indicated benefit from higher hardness for a loading sequence containing periodic compressive overloads. Similar benefit was not observed for CA loading.

The current work provided a qualitative analysis of mechanisms affecting fatigue improvement in HFMI-treated joints based on previous experimental observations [17,21]. The HFMI condition geometry was based on measurements, whereas the AW geometry was based on an assumption related to normal weld quality. It is

possible that the actual geometry change has been overestimated because of this. Availability of stress-strain data for HAZ and HFMI material conditions limited the accuracy with which the weld toe characteristics could be presented. In addition, the applied local properties represented estimated average behaviour of S700 steel. It is expected that the results are approximately applicable to other steels as a function of yield strength. Hardness measurements by Weich et al. [16] have indicated that the strain hardening effect of HFMI is higher for lower-strength steels than for higher-strength steels. This would mean that HFMI-treated steels with lower nominal yield strength than S700 could have higher local yield limit than what would be expected based on nominal  $f_y$ .

It is expected that there is significant variation in actual material properties, geometry and residual stress state of HFMI-treated welded joints, as indicated by the weld toe geometry and residual stress measurements in [21]. This was partly investigated in a preceding work by the authors [38], where the initial residual stress state, weld toe geometry and yield strength were varied. A decrease in compressive stress level, an increase in local stress concentration and a decrease in local yield strength all increased the calculated fatigue damage. The influence of different yield behaviours was not studied. Tehrani Yekta et al. [20] investigated the effect of different treatment parameters experimentally and numerically and concluded that the effectiveness of HFMI was not particularly sensitive to different treatment parameters. Simulating several material properties and test specimen geometries would be beneficial for confirming the qualitative results obtained in this work.

Taking into account the variation in the local effects of HFMI would give insight to the statistical variation in the resulting fatigue improvement. Before analysing this variation, however, the fatigue damage analysis needs to be further developed. The estimated  $P_{SWT}$  values for full HFMI were typically below  $0.8 \text{ MPa}^{0.5}$  indicating cycles to fatigue crack initiation greater than the range tested by Mikkola et al. [17], as shown by Fig. 7. As a result, the impact of residual stress relaxation, geometry improvement and strain hardening on resulting fatigue life is uncertain. Quantitative analysis of these effects was, however, out of the scope of the current work.

## 5. Conclusions

Residual stress relaxation and fatigue damage in HFMI-treated welded joints was investigated. The study is a part of a larger

research effort, where the fatigue performance, residual stress states, local geometry and local material properties of HFMI-treated S700 joints have been investigated experimentally. A transverse attachment was modelled considering the residual stresses, local geometry and local material properties in HFMI-treated and AW conditions. The HFMI-treated condition was modelled in three stages: (1) with compressive residual stresses at weld toe, (2) with compressive residual stresses and improved geometry at weld toe and (3) with compressive residual stresses, improved geometry and strain hardening at weld toe. All local properties were based on measured values. Relative fatigue damage was estimated from simulated local elastic-plastic stress-strain response using the Smith-Watson-Topper parameter. Main conclusions of the work are the following:

- The benefit from compressive residual stresses decreased with increasing stress range, stress ratio and peak load magnitude due to increasing level of residual stress relaxation. The simulations indicated full residual stress relaxation for  $R = 0.5$  and  $S_{\min} = -0.6f_y$ . First peak load was critical with respect to residual stress relaxation.
- Geometry improvement decreased the local stress concentration and thus the local stress range. This together with the increase in local yield strength due to strain hardening limited the level of residual stress relaxation. In addition, based on previous experimental results, strain hardening is expected to increase local fatigue resistance.
- Relative fatigue damage assessment showed benefit from HFMI with respect to AW condition even after residual stress relaxation for  $R = 0.5$  and  $S_{\min} \leq 0.6f_y$ . This is consistent with experimentally observed benefit from HFMI-treatment in welded joints subjected to high stress ratios and variable amplitude loading. Therefore, even though residual stress relaxation decreases the level of improvement from HFMI, benefit is expected to remain because of geometry improvement and strain hardening.

Notch stress analysis is proposed as future work to correlate the simulation results and experimental observations. In this way, residual stress relaxation and its effect on fatigue improvement in available fatigue data could be estimated.

## Acknowledgements

Support for this work has partially been provided by the Light and Efficient Solutions (LIGHT) and Breakthrough Steels and Applications (BSA) research programmes of the Finnish Metals and Engineering Competence Cluster (FIMECC) and the Finnish Funding Agency for Innovation (Tekes).

## References

- [1] Marquis GB, Barsoum Z. Fatigue strength improvement of steel structures by high-frequency mechanical impact: proposed procedures and quality assurance guidelines. *Weld World* 2014;58:19–28.
- [2] Marquis GB, Mikkola E, Yildirim HC, Barsoum Z. Fatigue strength improvement of steel structures by high-frequency mechanical impact: proposed fatigue assessment guidelines. *Weld World* 2013;57:803–22.
- [3] Yildirim HC, Marquis GB. Overview of fatigue data for high frequency mechanical impact treated welded joints. *Weld World* 2012;56:82–96.
- [4] Yildirim HC, Marquis GB. Fatigue strength improvement factors for high strength steel welded joints treated by high frequency mechanical impact. *Int J Fatigue* 2012;44:168–76.
- [5] Haagenen PJ, Maddox SJ. IIW recommendations on post weld improvement of steel and aluminium structures. Series in welding and other joining technologies, 79. Cambridge: Woodhead Publishing Ltd.; 2013.
- [6] Sonsino CM. Effect of residual stresses on the fatigue behaviour of welded joints depending on loading conditions and weld geometry. *Int J Fatigue* 2009;31:88–101.
- [7] Ghahremani K, Walbridge S. Fatigue testing and analysis of peened highway bridge welds under in-service variable amplitude loading conditions. *Int J Fatigue* 2011;33:300–12.
- [8] Mori T, Shimanuki H, Tanaka M. Effect of UIT on fatigue strength of web-gusset welded joints considering service condition of steel structures. *Weld World* 2012;56:141–9.
- [9] Okawa T, Shimanuki H, Funatsu Y, Nose T, Sumi Y. Effect of preload and stress ratio on fatigue strength of welded joints improved by ultrasonic impact treatment. *Weld World* 2013;57:235–41.
- [10] Kuhlmann U, Dürr A, Bergmann J, Thurmser R. Fatigue strength improvement for welded high strength steel connections due to the application of post-weld treatment methods (Effizienter Stahlbau aus höherfesten Stählen unter Ermüdungsbeanspruchung). Düsseldorf: FOSTA Research Association for Steel Applications; 2006.
- [11] Manteghi S, Maddox SJ. Methods for fatigue life improvement of welded joints in medium and high strength steels. Paris: International Institute of Welding; 2004 (IIW document XIII-2006-04).
- [12] Huo L, Wang D, Zhang Y. Investigation of the fatigue behaviour of the welded joints treated by TIG dressing and ultrasonic peening under variable-amplitude load. *Int J Fatigue* 2005;27:95–101.
- [13] McClung RC. A literature survey on the stability and significance of residual stresses during fatigue. *Fatigue Fract Eng Mater Struct* 2007;30:173–205.
- [14] Mikkola E, Doré MJ, Marquis GB, Khurshid M. Fatigue assessment of high-frequency mechanical impact (HFMI)-treated welded joints subjected to high mean stresses and spectrum loading. *Fatigue Fract Eng Mater Struct* 2015;38:1167–80.
- [15] Farajian-Sohi M, Nitschke-Pagel T, Dilger K. Residual stress relaxation of quasi-statically and cyclically-loaded steel welds. *Weld World* 2010;54:49–60.
- [16] Weich I, Ummenhofer T, Nitschke-pagel T, Dilger K, Eslami H. Fatigue behaviour of welded high strength steels after high frequency mechanical post-weld treatments. *Weld World* 2009;53:322–32.
- [17] Mikkola E, Marquis G, Lehto P, Remes H, Hänninen H. Material characterization of high-frequency mechanical impact (HFMI)-treated high-strength steel. *Mater Des* 2016;89:205–14.
- [18] Lihavainen V-M, Marquis GB. Fatigue life estimation of ultrasonic impact treated welds using a local strain approach. *Steel Res Int* 2006;77:896–900.
- [19] Leitner M, Simunek D, Shah SF, Stoschka M. Numerical fatigue assessment of welded and HFMI-treated joints by notch stress/strain and fracture mechanical approaches. *Adv Eng Softw* 2016;1–11. <http://dx.doi.org/10.1016/j.advengsoft.2016.01.022>.
- [20] Tehrani Yekta R, Ghahremani K, Walbridge S. Effect of quality control parameter variations on the fatigue performance of ultrasonic impact treated welds. *Int J Fatigue* 2013;55:245–56.
- [21] Yildirim HC, Marquis GB. A round robin study of high-frequency mechanical impact (HFMI)-treated welded joints subjected to variable amplitude loading. *Weld World* 2013;57:437–47.
- [22] Abaqus User Manual. Version 6.14 2014.
- [23] Weich I. Fatigue behaviour of mechanical post weld treated welds depending on the edge layer condition (Ermüdungsverhalten mechanisch nachbehandelter Schweißverbindungen in Abhängigkeit des Randschichtzustands) (Doctoral Thesis). Technischen Universität Carolo-Wilhelmina; 2008.
- [24] Barsoum Z, Jonsson B. Influence of weld quality on the fatigue strength in seam welds. *Eng Fail Anal* 2011;18:971–9.
- [25] Remes H. Strain-based approach to fatigue crack initiation and propagation in welded steel joints with arbitrary notch shape. *Int J Fatigue* 2013;52:114–23.
- [26] Bracke L, De Wispelaere N, Ahmed H, Güngör ÖE. S700MC/Grade 100 in heavy gauges: industrialisation at ArcelorMittal Europe. *Rev Métallurgie* 2011;108:323–30.
- [27] Remes H. Strain-based approach to fatigue strength assessment of laser-welded joints (Doctoral Thesis). Helsinki University of Technology; 2008.
- [28] Weich I. Edge layer condition and fatigue strength of welds improved by mechanical post-weld treatment. *Weld World* 2011;55:3–12.
- [29] Leitner M, Stoschka M, Eichlseder W. Fatigue enhancement of thin-walled, high-strength steel joints by high-frequency mechanical impact treatment. *Weld World* 2014;58:29–39.
- [30] Lemaitre J, Chaboche J-L. Mechanics of solid materials. Cambridge: Cambridge University; 1990.
- [31] Suominen L, Khurshid M, Parantainen J. Residual stresses in welded components following post-weld treatment methods. *Procedia Eng* 2013;66:181–91.
- [32] Smith R, Watson P, Topper T. A stress-strain function for the fatigue of metals. *J Mater* 1970;5:767–78.
- [33] Karakas Ö. Consideration of mean-stress effects on fatigue life of welded magnesium joints by the application of the Smith-Watson-Topper and reference radius concepts. *Int J Fatigue* 2013;49:1–17.
- [34] Liinalampi S, Remes H, Lehto P, Lillemäe I, Romanoff J, Porter D. Fatigue strength analysis of laser-hybrid welds in thin plate considering weld geometry in microscale. *Int J Fatigue* 2016;87:143–52. <http://dx.doi.org/10.1016/j.ijfatigue.2016.01.019>.
- [35] Marquis GB, Björk T. Variable amplitude fatigue strength of improved HSS welds. Paris: International Institute of Welding; 2008 (IIW Document XIII-2224-08).
- [36] Vanrostenberghe S, Clarin M, Shin Y, Droesbeke B, van der Mee V, Doré MJ, et al. Improving the fatigue life of high strength steel welded structures by



- post weld treatments and specific filler material (FATWELDHSS). Grant Agreement RFSR-CT-2010-00032. Luxembourg; 2015.
- [37] Soady KA. Life assessment methodologies incorporating shot peening process effects: mechanistic consideration of residual stresses and strain hardening Part 1 - effect of shot peening on fatigue resistance. *Mater Sci Technol* 2013;29:637–51.
- [38] Mikkola E, Remes H, Marquis GB. Influence of residual stresses on elastoplastic response in HFMI-treated welded joint under different load ratios. Paris: International Institute of Welding; 2015 (Document XIII-2591-15).